A method for inverse scattering based on the generalized Bremmer coupling series: Practical issues and examples

Alison E Malcolm*, Maarten V. de Hoop* and Henri Calandra†

* *Center for Wave Phenomena Colorado School of Mines, Golden, CO 80401, USA*

† *Total Exploration and Production, Geophysical Research Group 800 Gessner Suite 700 Houston, TX*

ABSTRACT

First order internal multiples are a source of coherent noise in seismic images. There are a number of techniques to estimate internal multiples in the data, but few methods exist that estimate imaging artifacts caused by internal multiples. We propose a method to do this in which the artifacts are estimated as part of the imaging process. Our technique is based on a hybrid of the Lippmann-Schwinger scattering series and the generalized Bremmer coupling series. Although we require knowledge of the velocity model this allows us to estimate internal multiples without assumptions inherent to other methods.

Key words: internal multiple attenuation, Bremmer series, downward continuation, imaging artifacts

1 INTRODUCTION

Internal multiples have been recognized as a problem in seismic experiments for a long time (Sloat, 1948). Although there are many techniques to attenuate these multiples in seismic data (Buttkus, 1979; Fokkema *et al.*, 1994; Berkhout & Verschuur, 1997; Verschuur & Berkhout, 1997; Weglein *et al.*, 1997; Jakubowicz, 1998; Kelamis *et al.*, 2002; ten Kroode, 2002; van Borselen, 2002) it is still not possible to estimate multiples in data with sufficient accuracy to remove all the errors they introduce in seismic images. Techniques like the angle-domain filtering proposed by (Sava & Guitton, 2005) are promising because they attenuate multiples directly in the image as opposed to in the data. In this way, even though the multiples are still not completely removed their location in the image is known. Thus, they are less likely to be misinterpreted as primary reflection energy. In this paper, we propose a technique for estimating imaging artifacts caused by internal multiples as part of the imaging process.

Fokkema & van den Berg (1993) use reciprocity to show the possibility of modeling surface-related multiples through a Neumann series expansion. Here, we use a related technique based on a hybrid of the Lippmann-Schwinger and Bremmer series to estimate internal multiples as part of the imaging process. Using a hybrid of the two series allows us to construct an inverse series following the ideas of the Lippmann-Schwinger series, while maintaining a structure consistent with the, convergent, Bremmer series. Because we estimate artifacts in the image rather than the data, we require knowledge of the velocity model. Technically this knowledge is necessary only to the depth of the shallowest reflector involved in the internal multiple (the depth of the up-to-down reflection). Our technique is similar to that of Jakubowicz (1998) in that it uses the techniques of so-called wave-equation migration to model internal multiples. Our method differs from Jakubowicz (1998) in that we propose to estimate the artifacts caused by first order internal multiples in the image rather than estimating the multiples in the data. In addition, Jakubowicz uses implicitly a version of the generalized Bremmer series (de Hoop, 1996) whereas we use a hybrid of the Lippmann-Schwinger and Bremmer series.

The Lippmann-Schwinger series is introduced by Lippmann (1956) to model particle scattering. In the

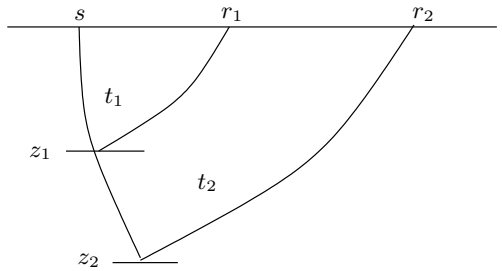

Figure 1. Illustration of the traveltime monotonicity assumption. The assumption states that if $z_1 < z_2$ then $t_1 < t_2$.

development of this series the wave-equation is solved in a known background model, with successive terms in the series being of successively higher order in the contrast operator. The contrast operator is the difference between the operator in the known background model and the true model. This idea is developed further by Moses (1956), and Prosser (1969); and Razavy (1975) where the series is developed for the quantum scattering problem. Weglein *et al.* (1997) uses this series to develop techniques for both surface and internal multiple attenuation; they choose water velocity as the known reference model. ten Kroode (2002) describes the mathematics behind this approach. In particular he notes that the suggested method requires two assumptions. The first assumption is that there are no caustics in the wavefield and the second is the so-called traveltime monotonicity condition. This condition is illustrated in Figure 1 and states that a wave excited at s and scattered at depth z_1 will arrive at the surface in less time than a wave following the same path from s to z_1, but scattering at z_2 instead, whenever z_1 is shallower than z_2.

The Bremmer series was introduced for planarly layered models by Bremmer (1951) and generalized to laterally heterogeneous models by de Hoop (1996). In the Bremmer series, the wavefield is split into up- and down-going constituents; these constituents are then coupled through reflection and transmission operators. Each term involves one more reflection/transmission and propagation step than the previous term. The first term of the series models direct waves, the second models singly scattered (where scattering may be reflection or transmission) waves and so on. The Bremmer series has been applied in many problems (see van Stralen (1997) for an overview) and the convergence of various generalizations of the original series has also been a subject of interest (Atkinson, 1960; Corones, 1975; Gray, 1983; McMaken, 1986). Aminzadeh & Mendel (1980; 1981) propose a method, using the Bremmer series, to attenuate surface-related multiples in a horizontally layered medium.

To estimate artifacts in the image caused by first-order internal multiples (FOIM), we proceed in two steps. We first develop a method to model FOIM, using the hybrid series; this is described in Section 2. Next, we use the modeled FOIM to estimate the artifacts they cause in the image, using ideas from the inverse series in Section 3. In Section 4 we describe an algorithm to perform these two steps at the same time. We illustrate the application of this algorithm to synthetic data in Section 5.

2 THE SCATTERING SERIES

We begin by decomposing the wavefield into its up- and down-going constituents. Following Stolk & de Hoop (2004a), we define

$$\mathsf{Q} = \frac{1}{2}\begin{pmatrix} (Q_+^*)^{-1} & -\mathcal{H}Q_+ \\ (Q_-^*)^{-1} & \mathcal{H}Q_- \end{pmatrix}, \tag{1}$$

where $\mathcal{H}$ denotes the Hilbert transform in time and * denotes adjoint. This operator relates the propagator for the full wave equation, G, to the propagator for the up-going one way equation, G_-, ($-$ denotes an up-going constituent and $+$ a down-going constituent) via

$$G = Q_-^* G_- \mathcal{H} Q_- \,. \tag{2}$$

The Q matrix, along with its inverse, diagonalizes the wave operator written as a first order system and thus splits the wavefield into its up- and down-going constituents. The wavefield in the diagonal system, $u_\pm$ is related to the full wavefield, u, via

$$u = Q_+^* u_+ + Q_-^* u_- \,, \tag{3}$$

applying the Q^{-1} matrix to the the vector $(u_+, u_-)^T$.

Denoting by U_j the vector $(u_{+,j}, u_{-,j})^T$ of up- and down-going wave constituents scattered j times, the terms in the hybrid forward scattering series are related by

$$\delta U_1(\widehat{V}) = D_t^2 \mathsf{L}_0(\widehat{V} U_0), \tag{4}$$

and

$$\delta U_m(\widehat{V}) = D_t^2 \mathsf{L}_0(\widehat{V}\delta U_{m-1}(\widehat{V})).$$

Here $\widehat{V}$ represents a matrix of reflectivities, and

$$\mathsf{L}_0 = \begin{pmatrix} G_+ & 0 \\ 0 & G_- \end{pmatrix} \tag{5}$$

denotes the matrix of one-way propagators evaluated in the background velocity model. We use a subscript 0 to indicate the field in the background model and δ to represent a contrast, thus the field U in the true medium is related to that in the background medium by $U = U_0 + \delta U$. Denoting by R the restriction of the wavefield to the acquisition surface (depth $z = 0$), we define $\mathsf{M}_0 = R\mathsf{Q}^{-1}\mathsf{L}_0$. The data are then modeled as

$$\delta D = \begin{pmatrix} d \\ \partial_z d \end{pmatrix} = -D_t^2 \mathsf{M}_0(\widehat{V}(U_0 + \sum_{m\in\mathbb{N}} (-1)^{m+1} \delta U_m(\widehat{V}))). \tag{6}$$

The leading order term on the right-hand side represents the singly scattered or Born contribution. This contribution is written explicitly in terms of the propagator H of the double-square-root (DSR) (Claerbout, 1985) equation as

$$\begin{aligned} d_1(s_0,r_0,t) &= \tfrac{1}{4}D_t^2 Q^*_{-,r_0}(0)Q^*_{-,s_0}(0) \\ &\quad \int_0^\infty \mathrm{d}z_1 H(0,z)Q_{-,r_1}(z_1)Q_{-,s_1}(z_1) \\ &\quad (E_1E_2a)(z_1,s_1,r_1,t_0)\,, \end{aligned} \tag{7}$$

where

$E_1 \quad : k(z,x) \mapsto \delta(r-s)k(z,\frac{r+s}{2})$,
$E_2 \quad : l(z,r,s) \mapsto \delta(t)l(z,r,s)$.

We denote by $a = 2c_0^{-3}\delta c$ the velocity contrast, in which c_0 denotes the smooth background velocity and δc denotes the velocity contrast. Together the E_1 and E_2 operators map the velocity contrast at depth to data at depth.

3 INVERSE SCATTERING

In inverse scattering the goal is to solve for $\widehat{V}$ in terms of the data d (cf. (6)). To this end, we assume that the contrast operator $\widehat{V}$ can be written as a series

$$\widehat{V} = \sum_{m\in\mathbb{N}} \widehat{V}_m(d)\,, \tag{8}$$

where $\widehat{V}_m$ is of order m in the data. Substituting this equation into (6) leads to the following relation between the $\widehat{V}_m(d)$,

$$D_t^2\mathsf{M}_0(\widehat{V}_m U_0) = D_t^4\mathsf{M}_0(\widehat{V}_{m-1}\mathsf{L}_0(\widehat{V}_1U_0))\,. \tag{9}$$

From this it follows that

$$-D_t^2\mathsf{M}_0(\widehat{V}U_0) = \delta D - \left(\sum_{m\in\mathbb{N}} D_t^2\mathsf{M}_0(\widehat{V}_m\delta U)\right)\,. \tag{10}$$

If we ignore the second term on the right-hand side, the problem of expressing $\widehat{V}$ in terms of the data reduces to inverse scattering in the Born approximation (Stolk & de Hoop, 2004b). In the context of wave-equation migration, the inverse scattering procedure is split into two parts: downward continuation and imaging.

We apply the adjoint propagator $H(0,z)^*$ to the modeled data in (7) yielding the downward continued data at depth z, for $t > 0$

$$\tilde{d}_1(z) = H(0,z)^* Q^*_{-,s}(0)^{-1}Q^*_{-,r}(0)^{-1}d\,. \tag{11}$$

This downward continuation uses the usual migration velocity model to estimate the data that would have been recorded at the depth z. Next, we apply the imaging condition to the downward continued data

$$a_1(z,.) = M\tilde{d}_1(z) \tag{12}$$

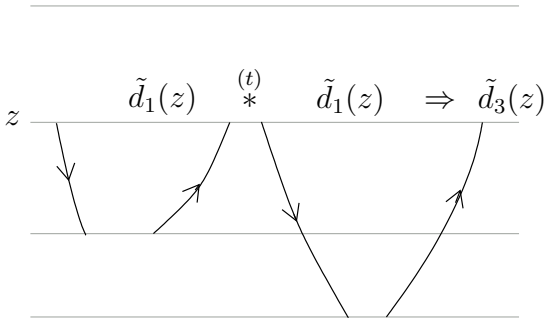

Figure 2. Illustration of equation 13, the estimation of the multiple at the depth z. The lines represent wavepaths rather than rays and do not connect as the imaging condition has not been applied.

where M is the imaging operator discussed by Stolk & de Hoop (Stolk & de Hoop, 2004a). We apply (11)-(12) to (10), from which we obtain an image (first term on the right-hand side) minus artifacts (second term). We compare our method with that of Weglein *et al.* (1997) and ten Kroode (2002) in Appendix B of Malcolm & de Hoop (2005).

The removal of negative times in the construction in (11) is an important step in our algorithm. It can also be computationally expensive to do this because windowing in time requires returning to the time domain. It is also this step that, in practice, imposes a limitation on the thickness of the multiple generating layer from which we can estimate multiples. To be able to attenuate internal multiples in a certain layer it is necessary to be able to remove the primary from the top of the layer without attenuating the reflection from the bottom of the layer.

4 ARTIFACTS DUE TO INTERNAL MULTIPLES IN IMAGING

First modeling internal multiples in the data and then constructing an estimate of the artifacts in the image is computationally expensive. The modeling step requires several propagation steps through the velocity model in addition to the cost of a depth migration needed to estimate artifacts in the image. To avoid these computational costs, we propose an algorithm summarized by the following flow chart

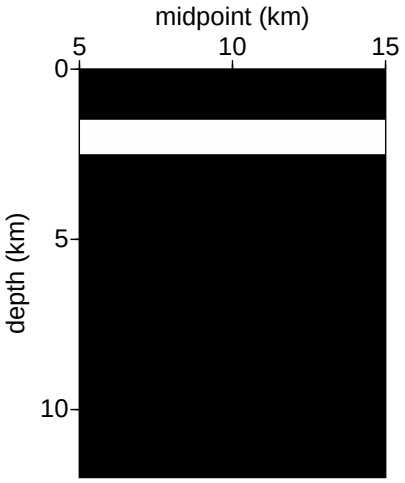

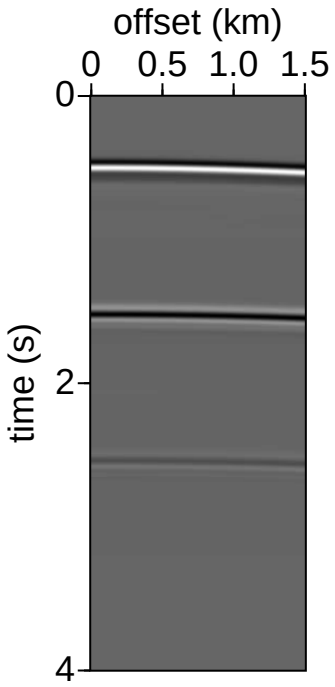

Figure 3. Top: Velocity model for flat example. Bottom: Surface data (CMP) for flat example.

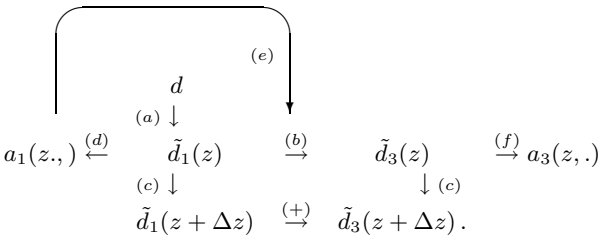

The algorithm can be divided into several steps. First, in (a), we downward continue the data to the depth z. Next we form an estimate, $a(z,x)$, of image from the data in (d). This estimate is used, in (b), to model the internal multiple downward continued to depth z via,

$$\tilde{d}_3(z,s,r,t) = D_t^2 \int Q^*_{-,s'}(z)(E_1 a)(z,s',r')Q^*_{-,r'}(z)$$
$$\tilde{d}_1(z,s',r,\cdot) \overset{(t)}{*} \tilde{d}_1(z,s,r',\cdot)\mathrm{d}s'\mathrm{d}r' \,. \tag{13}$$

Expression (13) is valid upon restricting $\tilde{d}_1$ to $t > 0$ and assumes a point source. If the point source assumption is not satisfied, an estimate of the wavelet should be deconvolved from the estimated multiple. Equation (13) is illustrated in Figure 2. Note the similarity between this expression and that used in the surface-related multiple elimination (SRME) procedure of Fokkema & van den Berg (1993) and Berkhout & Verschuur (1997). An estimate of the artifacts in the image is also made at the current depth in (f).

We then downward continue both the data and the estimated multiples to the next depth. To downward continue the multiples, d_3, we make use of the relation

$$d_3(s_0,r_0,t) = Q^*_{-,r_0}(0)Q^*_{-,s_0}(0)\int_0^\infty \mathrm{d}z H(0,z)\tilde{d}_3(z,.)\,, \tag{14}$$

which states that the multiple, d_3 can be estimated at the surface, $z = 0$ from the multiple, $\tilde{d}_3$ estimated at the depth z. Using relation (14) along with (11) we find that artifact in the image caused by FOIM at the depth z can be estimated by

$$a_3(z,.) = M\tilde{d}_3(z)\,, \tag{15}$$

the analog of (12). This step is (f) of the flowchart. The entire procedure is repeated for subsequent depths, with the estimated multiples at the depth $z+\Delta z$ being added to the multiples downward continued from depth z.

5 EXAMPLES

We begin with a simple, layered, example to illustrate the theory and then proceed to more complicated examples. The first example is a single layer, 1 km thick extending from 1.5 to 2.5 km, with a velocity of 2 km/s embedded in a homogeneous model with velocity 6 km/s.

Synthetic data were computed in this model with finite difference modeling, 101 midpoints were generated with 101 offsets at each midpoint and a spacing of 15 m in both midpoint and offset (we define offset as $(s-r)/2$); 4 seconds of data were recorded at 4 ms sampling. Figure 3 shows the velocity model and the modeled data.

In our method, the data are first downward continued as part of a standard wave-equation migration technique ((a) in the flowchart). The algorithm used to generate the examples shown here uses a pseudo-screen propagator with an implicit finite difference wide-angle correction (Jin *et al.*, 1998). In Figure 4 we show $\tilde{d}_1(z = 1.5)$, a single common-midpoint gather (cmp) downward continued to the depth $z = 1.5$ km of the top of the layer. The primary reflected from the top of the layer is located around $t = 0$, the reflection from the bottom of the layer at about $t = 1$ s and the first order internal multiple at about $t = 2$ s.

We now estimate the multiples at depth using (13). This requires restricting $\tilde{d}_1$ to time $t > 0$. The procedure removes the primary reflection from the current depth (which theoretically arrives at $t = 0$), in this case 1.5 km, before doing the convolution. If this process is not done correctly and energy remains at $t \leq 0$, all subsequent primaries will be duplicated in the estimated multiples section. In this model a simple time-windowing procedure is sufficient, because the reflections are far apart in time. In some situations, we find a τ-p filter to be more effective. This is because we typically see diffraction tails at small positive and negative times caused by the band-limited signal and imperfections in the imaging procedure. A τ-p filter is more effective at removing these tails when they are mixed with later reflections. Figure 4 show the results of applying the τ-p filter to the data.

Once the negative time contributions to the data have been removed, the multiple is estimated with (13), through a convolution with the data in a procedure similar to Surface Related Multiple Elimination (SRME) (Fokkema & van den Berg, 1993; Berkhout & Verschuur, 1997; Verschuur & Berkhout, 1997). The convolved wavefield is multiplied by an estimate of the image at the current depth, in this case $z = 1.5$ km (this is the $(E_1 a)(z, s', r')$ appearing in (13)). This completes (b) of the flowchart. The estimated multiple is shown in Figure 5. The event at about $t = 3$ s in the estimated multiple is a second-order internal multiple. This event is formed from the convolution of a primary with a first-order internal multiple. It is not present in the data panel because it arrives later than the final recorded time.

We now proceed to (c) of the flowchart and propagate both the data and the estimated multiples to the next depth. From the data, an image at the current depth is formed containing both primaries and multiples using (12) ((d) of the flowchart). Another image is also computed at the current depth, containing an estimate of the artifacts caused by FOIM, using (15) ((f) of the flowchart). The image containing both primaries and multiples gives the estimate of $a(z, x)$, which feeds back into the estimation of the multiples through (e) of the flowchart.

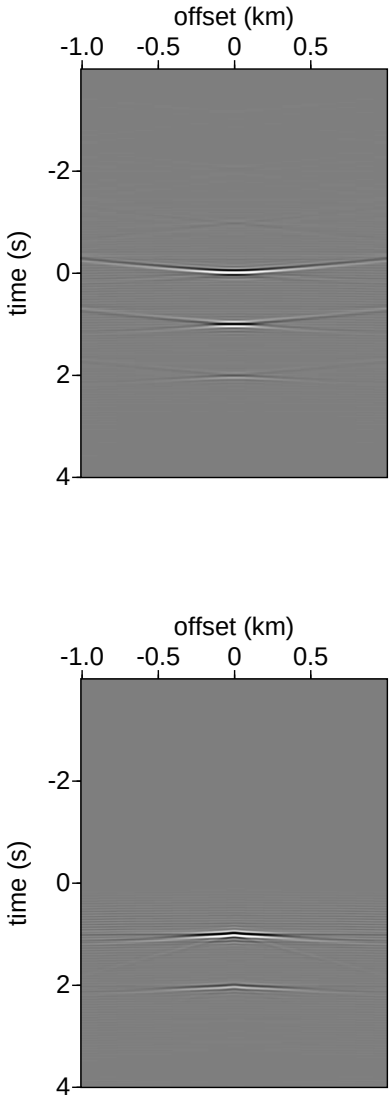

Figure 4. Data downward continued to the 1.5 km, the depth of the first reflector. Top: before the removal of the part of the data at $t \leq 0$. Bottom: after the removal of the part of the data at $t \leq 0$.

Figure 6 compares the estimated multiple to the true multiple. The estimated artifact aligns well with the artifact in the data, despite the fact that we have not accounted for the shape of the source wavelet. (Al-

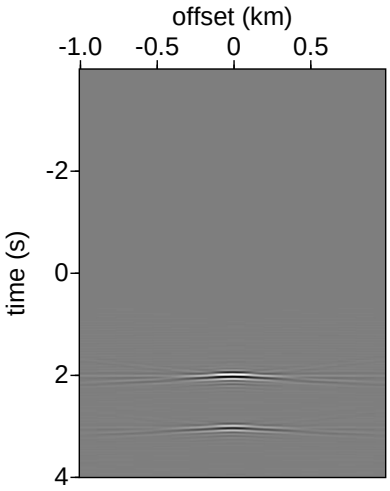

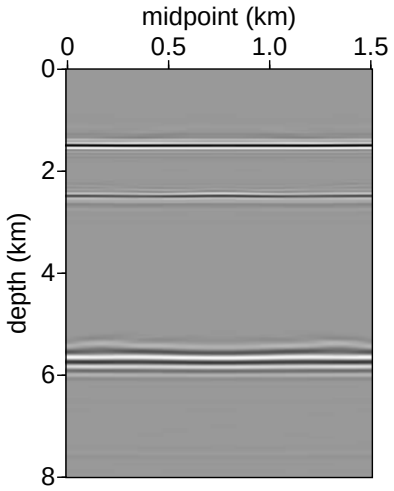

Figure 5. The estimated multiple, in the data, at a depth of 1.5 km; note the agreement with the true multiple in Figure 4.

though the wavelet has not been deconvolved, the data have been shifted so that the peak of the source wavelet is at zero time.)

To illustrate the ability of the method to estimate multiples in more complicated velocity models, we add a low-velocity lens to the model. The resulting velocity model is shown in Figure 7. The layer in this model is the same as the layer in the previous model except that it is 0.5 km deeper to allow more space for the low-velocity lens. The lens is located in the center of the model; it is circular with Gaussian velocity variations, a diameter of 600 m and a maximum contrast of -2 km/s. The addition of the lens has a large influence on the recorded data. A shot record directly above the lens is shown in Figure 8. Note the ringing, perhaps caused by numerical dispersion in the data modeling, that is particularly strong on the multiple. We use a double-square-root propagator that works in midpoint-offset coordinates rather than shot and receiver. To accommodate this choice, we use a subset of the available offsets so that each midpoint has the same number of offsets. The data from a midpoint of 9.8 km are shown in Figure 9. The first arrival is highlighted in this figure to show the triplications caused by the lens more clearly.

To estimate the multiple, we propagate the data to 2 km, the top of the layer, and again show the cmp at midpoint 9.8 km Figure 10 along with the estimated multiples at this depth. Note that the caustic has been removed by the propagation through the lens and that the multiple is accurately estimated. At this point, since

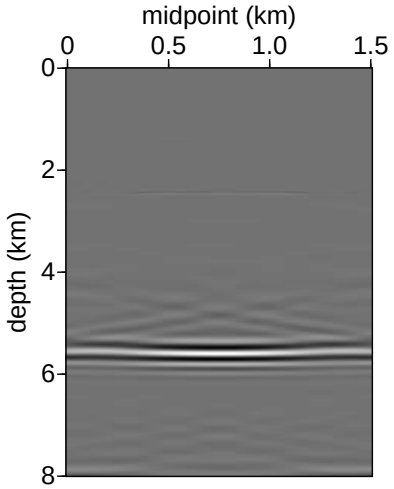

Figure 6. On the top is the image with an artifact from a first-order internal multiple at about 5.7 km depth. On the bottom is the estimated artifact.

we have removed the effects of the lens, the example is essentially the same as the flat case and the multiples are estimated accurately as is shown in Figure 11. Once again, the multiple is relatively weak in the estimated image. This is because of the residual moveout on the common image gather, which is shown in Figure 12.

To illustrate the dependence of this method on the background velocity model, we perturb the velocity in this section to ascertain the influence of the velocity on the final result. In theory, from equations (14) and (15),

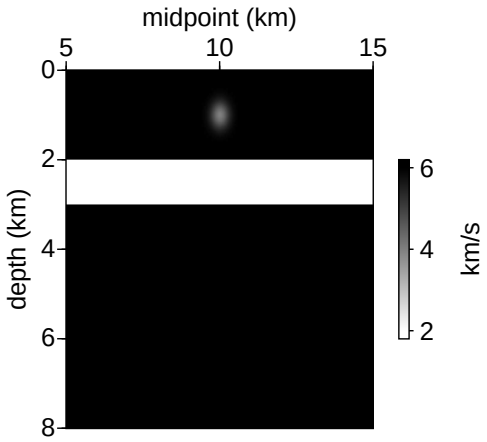

Figure 7. Velocity model, similar to the flat layered example discussed previously, with the addition of a low-velocity lens to demonstrate that the method works in laterally heterogeneous velocity models.

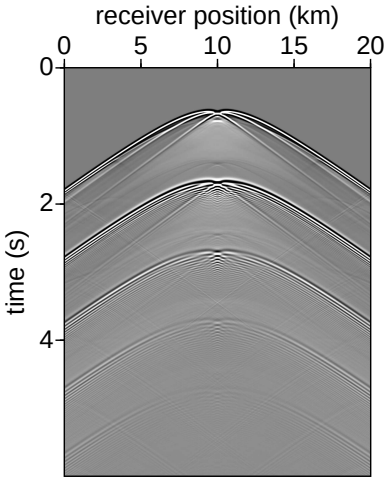

Figure 8. Shot record from $s = 10$ km, directly above the lens. Note the caustic introduced by the lens around zero-offset. The ringing on the second primary (at about 2 s) and the multiple (at about 3 s) is most likely numerical dispersion from the modeling of the data.

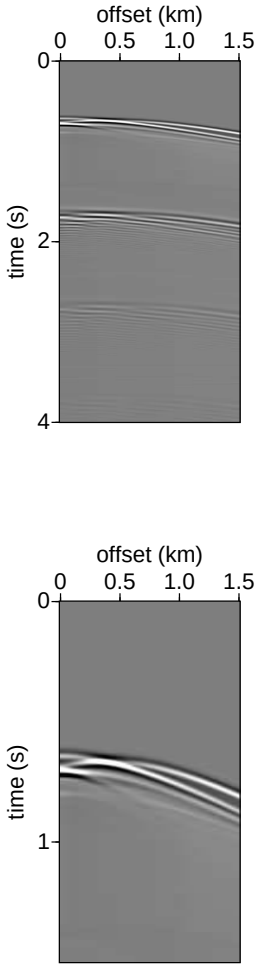

Figure 9. Common midpoint gather at 9.8 km, with only the offsets used to compute the images shown later. Note the triplications caused by the lens. Top: full gather. Bottom: zoom of the primary reflection from the top layer.

knowledge of the velocity is necessary only to the depth of the shallowest reflection, in this case the top of the layer at 2 km depth. To test this we perturb the model in two ways: first we make the layer thicker, and then we add a second lens, with properties identical to the first lens, below the layer. In the first case, we expect the multiple to be imaged at a shallower depth but otherwise to remain unchanged as the perturbation in the velocity is independent of midpoint. Figure 13 shows that we are still able to estimate the artifact accurately despite this error in the velocity model. There is more noise present in the image (left of Figure 13) here than in the correct velocity case (Figure 11). Part of the reason for this is that we have used a smaller agc window

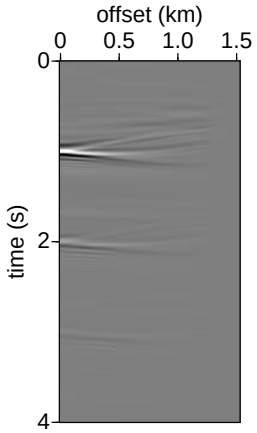

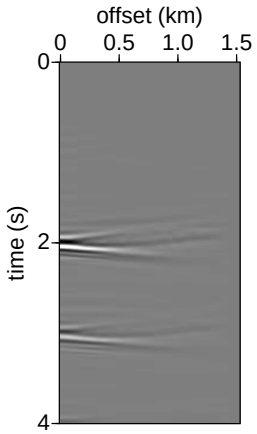

Figure 10. Top: Common midpoint gather at 9.8 km and 2 km depth. Note the disappearance of the multi-pathing as the data are now below the lens. Bottom: estimated multiples at this depth.

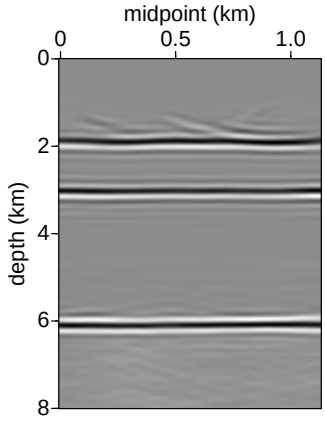

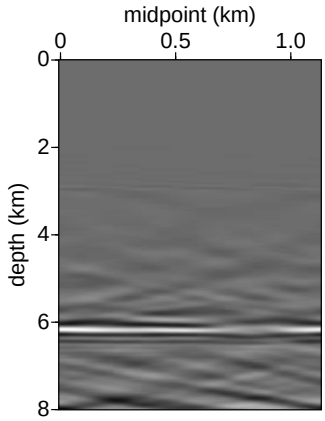

Figure 11. Top: Image with an artifact from the first-order internal multiple at approximately 6 km depth. Bottom: Estimated artifacts from first-order internal multiples.

to enhance the image of the bottom of the layer. In the second case, since the perturbation now depends on midpoint the estimated multiple also depends on midpoint. Although the estimated artifact does not match the image artifact as well in this case as when the correct velocity is used, the estimate remains quite good, as shown in Figure 14.

The theory presented here does require knowledge of the velocity model to the depth of the up to down reflection (top of layer at 2 km depth). To test the sensitivity of the method to errors in this velocity, we remove the lens and estimate the image and the multiple in this incorrect velocity model. The results are shown in Figure 15. Although the estimated artifact remains at roughly the correct depth, there is a phase difference between it and the actual artifact and the variation in the image with midpoint is not accurately estimated. Removing the lens entirely is a large change in the model and thus we expect a large change in the image. In Figure 16, we demonstrate that we can still estimate the multiple with reasonable accuracy when the velocity perturbation is less dramatic. In this case the lens has been moved 0.2 km shallower than in the true velocity model, and with the exception of the phase change between the artifact and our estimate, the result is still good.

The next synthetic model is based on a Shell field in the North Sea. The velocity model is a 2D slice of a 3D velocity model with the steeply dipping reservoir interval added manually. The velocity model is shown in Fig-

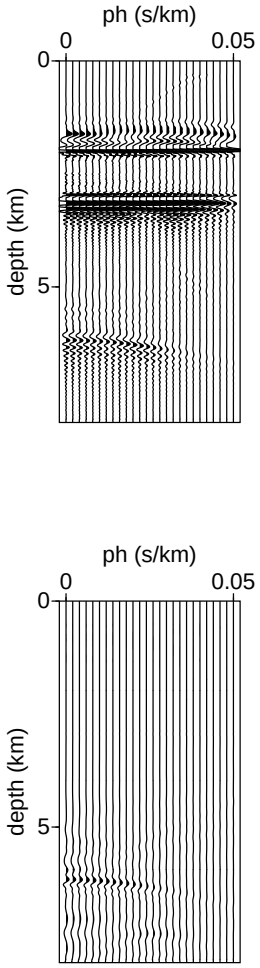

Figure 12. Common image gathers for midpoint 9.8 km. Top: image with artifact. Bottom: estimated artifact.

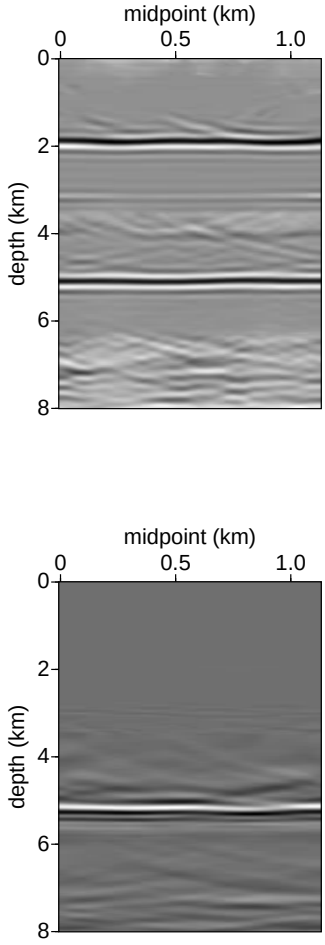

Figure 13. In these images, the reflector has been extended to 3.5 km from 3 km to test the sensitivity of the method to the velocity model. Top: Image with artifacts from internal multiples. Bottom: Estimated artifacts from first-order internal multiples.

ure 17; the chalk layer beginning at about 3 km depth is expected to be the largest generator of internal multiples because of the strong velocity contrast between the chalk and surrounding layers. Some of the layers discussed later are labeled on this figure. The acquisition was designed to simulate a marine experiment. A total of 601 shots were computed with finite differences at a 25 m increment beginning at 15 km and continuing to 30 km. The streamer consists of 241 receivers (hydrophones) spaced at 25 m increments beginning with zero-offset. For the tests shown here we use a subset of 241 midpoints, beginning at 15 km with a spacing of 50 m, with 31 offsets at 50 m spacing beginning at zero-offset. A total of 6 s of data were computed with a 4 ms time sampling interval. A small subset of the available offsets were used to avoid imaging refracted waves visible at long offsets, and to avoid to the extent possible numerical dispersion, which is stronger at larger offsets.

In Figure 18, the data are shown downward continued to a depth of 2.5 km, just above the top of the chalk (the chalk layer is labeled in Figure 17). This figure illustrates that in this instance a simple time windowing is not sufficient. Instead we use a τ-p filter to attenuate the reflection from the top of chalk. By using a τ-p filter rather than a simple time windowing we are also able to apply the filter less frequently as it allows us to remove the entire top of chalk reflection at once, from above the chalk layer.

Figures 19 and 20 compare the estimated artifacts to the true artifacts in the image. The multiples were es-

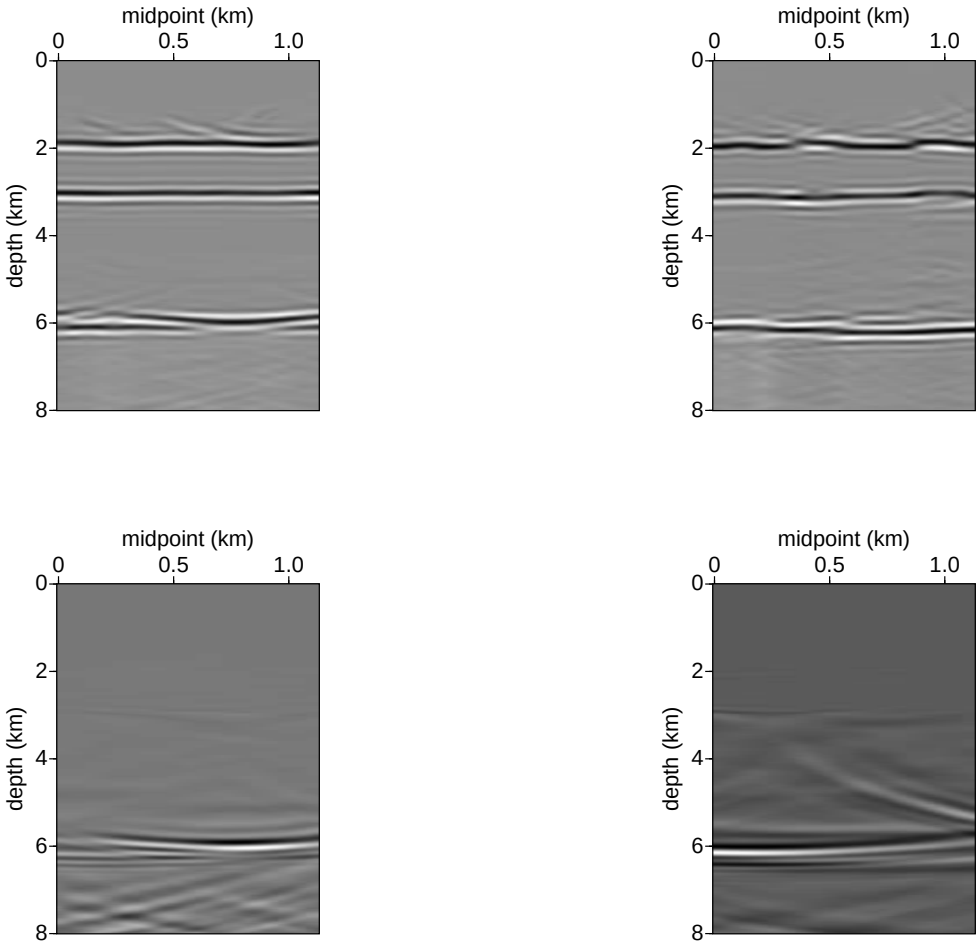

Figure 14. In these images, a second lens has been added beneath the layer to introduce a laterally varying velocity perturbation. Top: Image with artifacts from internal multiples. Bottom: Estimated artifacts from first-order internal multiples.

Figure 15. The lens was removed from the velocity model before generating these images. Because this perturbation is above the top of the layer, we expect this to have an impact on the estimated multiple. Note the change in the accuracy of the estimate beneath the lens. Top: Image with artifacts from first-order internal multiples. Bottom: Estimated artifacts from first-order internal multiples.

timated in a depth window from 2.5 to 4.2 km depth and the τ-p filter was applied at 2.5 and 3.25 km. Thus we expect to see the multiples from the top and bottom of the chalk layer. The estimated multiples are imaged at approximately the depth expected based on the velocity model. The multiple at about 4.5 km depth is imaged at the depth expected for an internal multiple entirely within the chalk layer extending from approximately 3 to 4 km depth. The multiples at about 5.5 km are either peg-legs from the bottom of the chalk and the bottom of layer 2 or internal multiples with both deeper scattering points at the bottom of the layer 2. The artifacts caused by these multiples in the image are not easy to see, however, as they are obscured by other ringing in the data. This ringing does not appear in the estimated artifacts because these estimates are made using the primaries, which arrive at earlier times and are thus less strongly influenced by the ringing. To highlight the multiples as much as possible, we have stacked only the smallest p-values (i.e. the first few traces of the common image gather) to make the image and we have low-passed filtered the image to remove as much of the high-frequency noise visible after the chalk layer as possible, without damaging the imaged structure. In Figure 20 we compare our estimate to one made by ten Kroode (2005), in which he estimates the multiples from the top of the

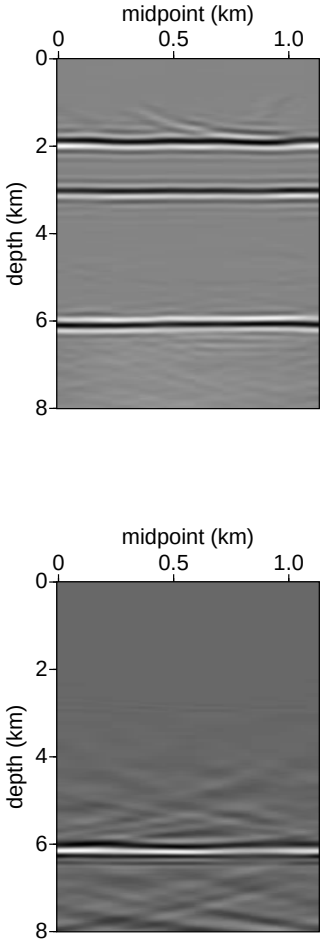

Figure 16. In this model the lens was moved 0.2 km deeper than in the correct velocity model. Because this perturbation is above the top of the layer, we expect this to have an impact on the estimated multiple. Note the phase difference between the estimated artifact and the image. Top: Image with artifacts from first-order internal multiples. Bottom: Estimated artifacts from first-order internal multiples.

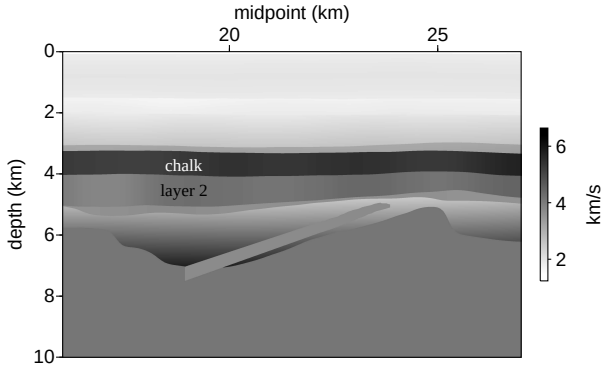

Figure 17. Velocity model for the North Sea example.

chalk layer and compares them to the multiples in the data. This is an extremely coarse comparison as it is not possible to show his image, but the arrows indicate several locations at which artifacts from multiples are present in his image.

6 DISCUSSION

We have described a method to estimate imaging artifacts caused by first-order internal multiples. This method requires knowledge of the velocity model down to the top of the layer that generates the multiple (the depth of the up-to-down reflection). The main computational cost of the algorithm comes from the propagation of the data and the internal multiples. Because two data sets are propagated (the data themselves and the estimated multiples), the cost of the algorithm described here is about twice that of a usual pre-stack depth migration, plus the cost of the removal of negative times. The removal of negatives times can be expensive because it is necessary to return all of the data to the time domain to window the data. Using the τ-p filter reduces this cost because the negative times can be removed less frequently, although the cost of the τ-p transform is much higher than that of a simple time windowing. By estimating the multiple in depth rather than in the data, we avoid difficulties caused by caustics in the wavefield or the failure of the traveltime monotonicity assumption. In addition, estimating artifacts in the image rather than estimating multiples in the data shows clearly which part of the image has been contaminated by internal multiples, even if those multiples are poorly estimated or incompletely subtracted.

7 ACKNOWLEDGMENTS

We thank Total for permission to publish the real data example. We are grateful to Fons ten Kroode and Shell for the North Sea synthetic example. We also appreciate the many helpful discussion with Kris Innanen and Ken Larner as well as the coding assistance from Peng Sheng, Feng Deng, Linbin Zhang and Dave Hale. This work was supported by Total and the sponsors of the Consortium Project on Seismic Inverse Methods for Complex Structures at the Center for Wave Phenomena.

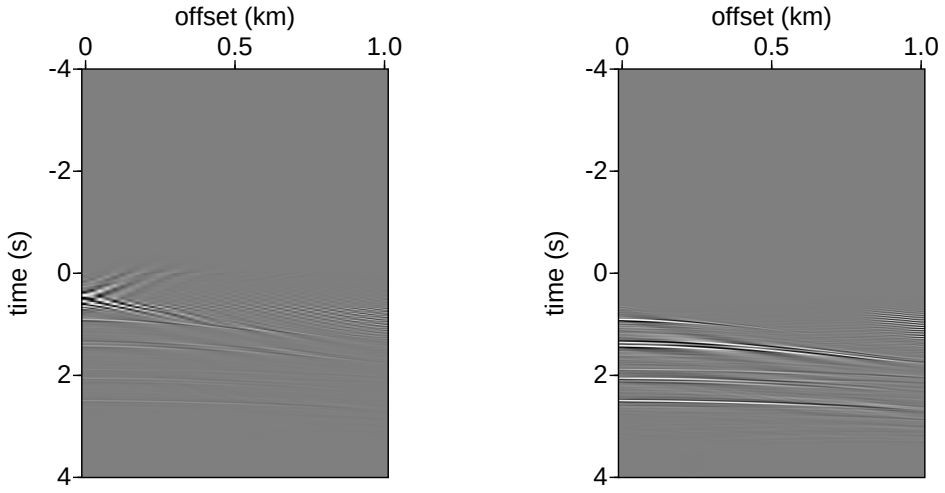

Figure 18. Data downward continued to a depth of 2.5 km. Left: before the removal of the part of the data at $t \leq 0$. Right: after the removal of the part of the data at $t \leq 0$ using a τ-p filter.

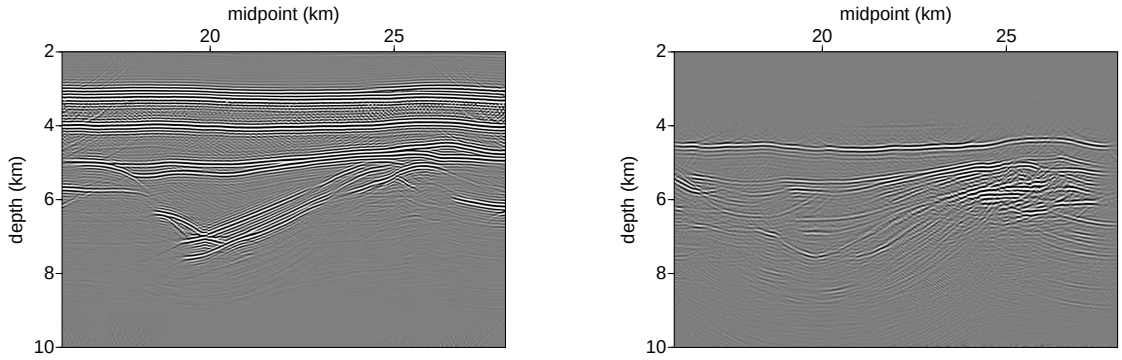

Figure 19. On the left is the image with an artifact from a first-order internal multiple at about 4.5 km depth. On the right is the estimated artifact.

REFERENCES

Aminzadeh, F., & Mendel, J. M. 1980. On the Bremmer series decomposition: Equivalence between two different approaches. *Geophysical Prospecting*, **28**, 71–84.

Aminzadeh, F., & Mendel, J. M. 1981. Filter Design for suppression of surface multiples in a non-normal incidence seismogram. *Geophysical Prospecting*, **29**, 835–852.

Atkinson, F. V. 1960. Wave propagation and the Bremmer series. *J. Math. Anal. Appl.*, **1**, 225–276.

Berkhout, A. J., & Verschuur, D. J. 1997. Estimation of multiple scattering by iterative inversion, Part I: Theoretical considerations. *Geophysics*, **62**(5), 1586–1595.

Bremmer, H. 1951. The W. K. B. approximation as the first term of a geometric-optical series. *Communications on Pure and Applied Mathematics*, **4**, 105–115.

Buttkus, B. 1979. Coherency weighting – an effective approach to the suppression of long leg multiples. *Geophys. Prosp.*, **27**, 29–39.

Claerbout, J. F. 1985. *Imaging the Earth's Interior*. Blackwell Sci. Publ.

Corones, J. P. 1975. Bremmer series that correct parabolic approximations. *J. Math. Annal. Appl.*, **50**, 361–372.

de Hoop, M. V. 1996. Generalization of the Bremmer coupling series. *J. Math. Phys.*, **37**, 3246–3282.

Fokkema, J. T., & van den Berg, P. M. 1993. *Seismic appli-*

cations of acoustic reciprocity. Amsterdam: Elsevier.
Fokkema, J.T., Van Borselen, R. G., & Van den Berg, P.M. 1994. *Removal of inhomogeneous internal multiples*. Eur. Assn. of Expl. Geophys. Page Session:H039.
Gray, S. H. 1983. On the convergence of the time domain Bremmer series. *Wave Motion*, **5**, 249–255.
Jakubowicz, H. 1998. Wave equation prediction and removal of interbed multiples. *Pages 1527–1530 of: Expanded Abstracts*. Soc. Explor. Geophys.
Jin, Shengwen, Wu, Ru-Shan, & Peng, Chengbin. 1998. Prestack depth migration using a hybrid pseudo-screen propagator. *SEG Technical Program Expanded Abstracts*, **17**(1), 1819–1822.
Kelamis, P., Erickson, K., Burnstad, R., Clark, R., & Verschuur, D. 2002. *Data-driven internal multiple attenuation - Applications and issues on land data*. Soc. of Expl. Geophys. Pages 2035–2038.
Lippmann, B. A. 1956. Rearrangement Collisions. *Phys. Rev.*, **102**(1), 264–268.
Malcolm, A. E., & de Hoop, M. V. 2005. A method for inverse scattering based on the generalized Bremmer coupling series. *submitted to Inverse Problems, CWP-486*.
McMaken, H. 1986. On the convergence of the Bremmer series for the Helmholtz equation in 2d. *Wave Motion*, **8**, 277–283.
Moses, H. E. 1956. Calculation of scattering potential from reflection coefficients. *Phys. Rev.*, **102**, 559–567.
Prosser, R. T. 1969. Formal solutions of inverse scattering problems. *Journal of Math. Phys.*, **10**, 1819–1822.
Razavy, M. 1975. Determination of the wave velocity in an inhomogeneous medium from reflection data. *J. Acoust. Soc. Am.*, **58**, 956–963.
Sava, Paul, & Guitton, Antoine. 2005. Multiple attenuation in the image space. *Geophysics*, **70**(1), V10–V20.
Sloat, John. 1948. Identification of echo reflections. *Geophysics*, **13**(1), 27–35.
Stolk, C. C., & de Hoop, M. V. 2004a. Modeling of seismic data in the downward continuation approach. *submitted to SIAM J. Appl. Math.* CWP468P.
Stolk, C. C., & de Hoop, M. V. 2004b. Seismic inverse scattering in the downward continuation approach. *submitted to SIAM J. Appl. Math.* CWP469P.
ten Kroode, A. P. E. 2002. Prediction of internal multiples. *Wave Motion*, **35**, 315–338.
ten Kroode, A. P. E. 2005. personal communication.
van Borselen, R. 2002. Data-driven interbed multiple removal: Strategies and examples. *In: Expanded Abstracts*. Society of Exploration Geophysicists.
van Stralen, M. J. N. 1997. *Directional decomposition of electromagnetic and acoustic wave-fields*. Ph.D. thesis, Delft University of Technology.
Verschuur, D. J., & Berkhout, A. 1997. Estimation of multiple scattering by iterative inversion, Part II: Practical aspects and examples. *Geophysics*, **62**(5), 1596–1611.
Weglein, A., Gasparotto, F. A., Carvalho, P. M., & Stolt, R. H. 1997. An inverse-scattering series method for attenuating multiples in seismic reflection data. *Geophysics*, **62**, 1975–1989.

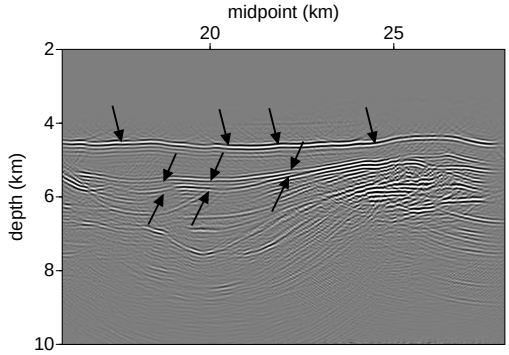

Figure 20. This figure repeats the estimated artifacts from internal multiples shown in Figure 19, with arrows indicating locations at which multiples can be observed in the results of ten Kroode (2005).